JGR Space Physics

Key Points:
- The Swarm mission provides global climatological maps of ionospheric plasma irregularities
- Ionospheric plasma irregularities at all latitudes depend on the IMF Bz and solar activity
- At low latitudes, the variability of the ionosphere is low on average, but extreme events result in large structuring

Supporting Information:
- Supporting Information S1
- Movie S1

Correspondence to:
Y. Jin,
yaqi.jin@fys.uio.no

Ionospheric Plasma Irregularities Based on In Situ Measurements From the Swarm Satellites

Yaqi Jin[1] [iD], **Chao Xiong**[2] [iD], **Lasse Clausen**[1] [iD], **Andres Spicher**[1] [iD], **Daria Kotova**[1] [iD], **Steffen Brask**[1] [iD], **Guram Kervalishvili**[2] [iD], **Claudia Stolle**[2] [iD], **and Wojciech Miloch**[1] [iD]

[1]Department of Physics, University of Oslo, Oslo, Norway, [2]Helmholtz Centre Potsdam, GFZ German Research Centre for Geosciences, Potsdam, Germany

Abstract In this study, we present global climatological distributions of ionospheric plasma irregularities based on measurements by the Swarm satellites. These first global statistics obtained by direct, in situ measurements of plasma variations with Swarm confirm the presence of three main regions of strong ionospheric irregularities: the magnetic equator extending from postsunset to early morning, in the auroral ovals (from dayside cusp to nightside), and inside the polar caps. At equatorial latitudes, ionospheric irregularities form two bands of enhanced plasma fluctuations centered around ±10° magnetic latitude. Due to different plasma processes, ionospheric irregularities at high and low latitudes show different distributions. Though the averaged intensity of plasma irregularities is weaker at equatorial latitudes than at high latitudes, the occurrence rate of significant plasma fluctuations (corresponding to extreme events) is much higher at the equator than that at high latitudes. Equatorial irregularities display clear seasonal and longitudinal variations; that is, they are most prominent over South America during the December solstice and are located over Africa during the June solstice. The magnitude of ionospheric irregularities at all latitudes is strongly controlled by the solar activity. Ionospheric irregularities become significantly weaker after 2016 during the current declining phase of solar activity. The interplanetary magnetic field Bz modulates the occurrence of ionospheric irregularities at both high and low latitudes.

1. Introduction

Irregularities in the ionospheric plasma density impact the propagation of radio waves (Hey et al., 1946). They can lead to rapid fluctuations in the amplitude and phase of trans-ionospheric radio waves received on the ground. These effects are termed as ionospheric scintillations (e.g., Basu & Groves, 2001; Yeh & Liu, 1982). The phase screen theory relates scintillations to plasma irregularities, where, for example, the variance of phase fluctuations σ_ϕ^2 is proportional to the variance in the electron density fluctuations $\sigma_{\Delta n}^2$ (Booker et al., 1950; Rino, 1979; Yeh & Liu, 1982), where Δn is the variation of the electron density. For significant effects on amplitude scintillations, the plasma irregularities should have a scale size of the order of the Fresnel radius, that is, ca. 400 m for the Global Navigation Satellite System (GNSS) signals by assuming the phase screen within a thin slab located at ~350 km altitude. Thus, amplitude scintillations depend on both the thickness of the scintillation layer and the structuring of the ionosphere in that layer.

Scintillations of received GNSS signals can severely impact the performance of such systems (e.g., Datta-Barua et al., 2014; Kintner & Ledvina, 2005; Kintner et al., 2007). Since modern society relies increasingly on GNSS, such as Global Positioning System (GPS), GLONASS or Galileo, and satellite-based communication systems, a good insight into the distribution of irregularities would be beneficial for the reliability of such systems. One example would be applications based on precise positioning and timing with GNSS. In the last decades, the ground-based observation stations have been expanded significantly, in particular in the northern hemisphere, and our knowledge on the distribution of ionospheric irregularities is steadily advancing.

The global occurrence of ionospheric irregularities (and the resulting scintillations) has been initially summarized based on the data from the ground-based receivers. Figure 1 shows a global scintillation distribution which is replicated from Basu, Mackenzie, and Basu (1988). One can see "three major regions of significant scintillations, i.e., a region around the magnetic equator in the postsunset period, the nightside auroral oval and dayside cusp, and a region within the polar cap at all local times" (Basu, Mackenzie, & Basu, 1988). This
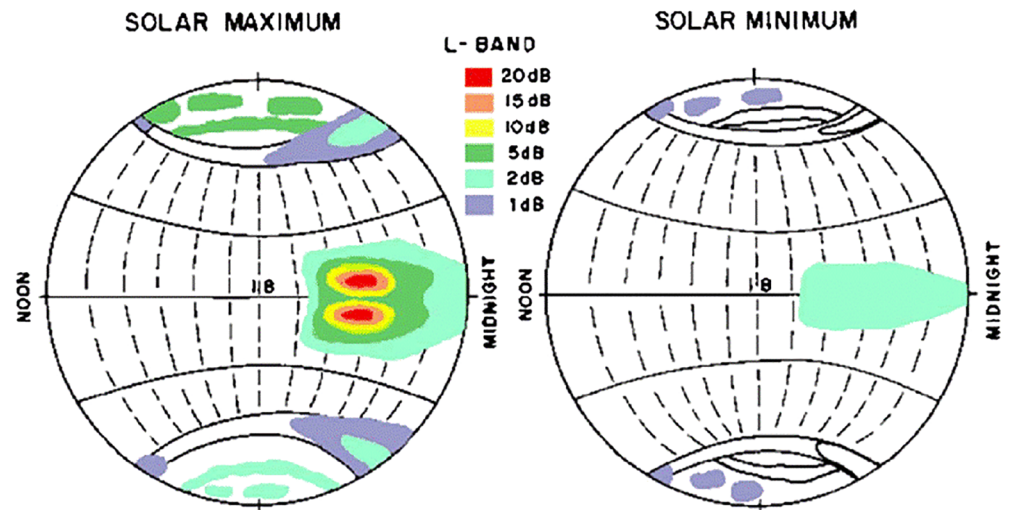
Figure 1. The global characteristics of ionospheric scintillations during the solar maximum and solar minimum in terms of the power fade as summarized by Basu, Mackenzie, and Basu (1988).

widely accepted view of the scintillation distribution has been obtained using only five ground-based receivers measuring very high frequency (VHF) scintillations and thus related to kilometer-scale irregularities. To date, only limited statistical studies have been performed (Prikryl et al., 2015; Spogli, Alfonsi, Cilliers, et al., 2013; Spogli, Alfonsi, Romano, et al., 2013), and none have been thorough enough to confirm that these statistics apply to both solar minimum and maximum and at all geographic latitudes and longitudes. To confirm such statistics, a study would require utilizing satellite-based measurements, and it should emphasize interhemispheric asymmetries due to geometry of the Earth magnetic field. We note that the radio occultation technique has also been used to study ionospheric irregularities (Ko & Yeh, 2010; Uma et al., 2012). However, the studies of high-latitude irregularities using radio occultations are still rare (Hocke et al., 2019).

Plasma irregularities and corresponding plasma structuring at different latitudes are due to different dynamic processes. At high latitudes, ionospheric irregularities are related to such phenomena as polar cap patches (Jin et al., 2014; Mitchell et al., 2005), cusp aurora (Jin et al., 2015, 2017; Oksavik et al., 2015), substorms (Hosokawa et al., 2014; Jin et al., 2014), or auroral blobs (Jin et al., 2016). At low latitudes, the most prominent phenomenon that creates ionospheric scintillations is the equatorial spread F (ESF), which is a hierarchy of ionospheric irregularities developing after sunset (Farley et al., 1970; Woodman & La Hoz, 1976). Associated with ESF are equatorial plasma bubbles or equatorial plasma depletions (EPD)—low-density regions as compared to the surrounding ionosphere, which are associated with significant plasma structuring (Stolle et al., 2006; Woodman & La Hoz, 1976). Another class of ionospheric structures often observed at low latitudes, and which can also lead to scintillations, are plasma blobs that are plasma density enhancements with respect to ambient plasma (Huang et al., 2014; Kil et al., 2019; Park et al., 2003; Wang et al., 2019). All these phenomena and associated plasma structuring are widely accepted as main sources of scintillation of trans-ionospheric radio waves.

One can expect that the distribution of plasma irregularities is largely controlled by external drivers, such as the solar wind conditions, and as such, they are also related to the solar activity. Local variations due to the geometry of magnetic field are also expected. However, to our knowledge, the global climatology of ionospheric irregularities, which takes into account different latitudes and longitudes, and their characterization that is derived from a single platform, has not been carried out in one study so far. In this work, we address this problem with a new comprehensive dataset from the European Space Agency's Swarm satellites.

Our advantage is that Swarm, as Low Earth Orbit (LEO) polar satellites, gives us an opportunity to study plasma irregularities in situ, and the length of the mission can provide global statistics of plasma

irregularities, including both their amplitudes, variability, and scale sizes along the satellite tracks over more than half of the solar cycle. This opens for a possibility to study the detailed statistics of plasma irregularities from ~7–15 km scales, thus slightly larger scales than those giving rise to the scintillations considered in Basu, Mackenzie, and Basu (1988). Furthermore, a detailed study of their dependence on external drivers, such as solar activity, or the interplanetary magnetic field (IMF), can be carried out at selected geomagnetic latitudes. As such, the in situ statistics by satellites give an invaluable insight into the nature of plasma irregularities and consequently can shed light onto scintillating properties of the ionosphere and facilitate scintillation modeling, especially those from the global perspective.

In this work, we use the in situ electron density data from the Swarm satellites to establish and analyze climatological maps of ionospheric irregularities at all latitudes, longitudes, and local times and discuss them in the context of previous studies. Since the Swarm orbits are close to the F2 peak of the ionosphere and the F2 layer contributes most to the ground scintillation data (e.g., Aarons, 1993), it is possible to relate the Swarm in situ measurements of the electron density to scintillations experienced on the ground (however, it is not a bi-implication, as we discuss later). We further analyze the occurrence in the context of the solar activity and driving by the solar wind and IMF.

2. Data and Methodology

Swarm is a constellation of three identical satellites (Swarm A, B, and C) that were launched on 22 November 2013 into near-polar orbits with an initial altitude of around 500 km (e.g., Lühr et al., 2015; Olsen et al., 2013). From January to April 2014, the orbits were maneuvered such that Swarm B was raised to around 520 km, while Swarm A and C fly side by side at around 470 km with a difference in longitude by approximately 1.4°. Due to a different precession rate, the orbital plane of Swarm B deviates gradually from those of Swarm A and C. In this study, we only show data from Swarm A, as the results from the other two satellites show similar features. Due to the orbital altitude variation of Swarm A (see the supporting information), we use data from April 2014 to April 2019 for constructing statistics in sections 3.3 and 3.4. However, we use all available data (December 2013 to October 2019) in section 3.4 for presenting the long-term variations (i.e., from late 2013 up to the third quarter of year 2019). Thus, our study corresponds to nearly 6 years of the declining solar activity and gives an opportunity for studies of both seasonal and annual variations of plasma irregularities.

Each of the Swarm spacecraft carries an Electric Field Instrument (EFI) (Knudsen et al., 2017). The EFI includes the Thermal Ion Imager and two Langmuir probes. With the Langmuir probes, the in situ electron density (Ne) can be measured by Swarm at a rate of 2 Hz. The in situ electron density can be successfully used in detecting and characterizing ionospheric structures and irregularities, such as polar cap patches at high latitudes (Jin, Spicher, et al., 2019; Spicher et al., 2015, 2017). Recently, several derived plasma density parameters have been produced as a part of the Swarm IPIR project, and are available as Ionospheric Plasma Irregularities (IPIR) data product (https://earth.esa.int/web/guest/missions/esa-eo-missions/swarm/activities/scientific-projects/disc#IPIR) (Jin, Spicher, et al., 2019). IPIR consists of ca. 30 entries based on data from the Langmuir probes, GPS receivers, and magnetometers onboard Swarm. IPIR allows for a comprehensive characterization of plasma density variations along the Swarm trajectories allowing for a global statistical study.

In this work, we focus on in situ density measurements and use the following parameters, which are a part of the IPIR data product: rate of change of density (ROD) and rate of change of density index (RODI).

ROD is defined as a time derivative of the electron density:

$$ROD(t) = \frac{Ne(t + \Delta t) - Ne(t)}{\Delta t}$$

Here $\Delta t = 0.5$ s because we use 2 Hz Swarm data to account for small-scale fluctuations.

RODI is the standard deviation of ROD in a running window of 20 s:

$$RODI(t) = \sqrt{\frac{1}{N-1} \sum_{t_i=t-\Delta t/2}^{t_i=t+\Delta t/2} \left| ROD(t_i) - \overline{ROD} \right|^2}$$

where $\overline{ROD}$ is the mean of $ROD(t_i)$:

$$\overline{ROD} = \frac{1}{N} \sum_{t_i=t-\Delta t/2}^{t_i=t+\Delta t/2} ROD(t_i)$$

where $\Delta t = 20$ s. Therefore, the unit of RODI is cm^{-3}/s. In this way, RODI is a measure of the electron density fluctuations at spatial scales of about 7.5–150 km.

Where applicable, we also use the Total Electron Content (TEC) in the topside ionosphere derived from the Swarm onboard GPS receiver, Swarm derived field-aligned currents, and so forth. To assess the solar activity, we use the F10.7 index, which measures the total emission at a wavelength of 10.7 cm of the solar disk, and which is widely used for this purpose (Tapping, 2013).

3. Results

3.1. Example of Ionospheric Irregularities

We start from presenting an example of the Swarm observations and how our derived parameters can help identifying particular structures in the ionosphere. Figure 2 shows results obtained during one half orbit (descending node) of Swarm A. The global map of the TEC at 17 UT, 8 September 2017 is presented in Figure 2a. This is a global ionosphere map (GIM) produced by the Center for Orbit Determination in Europe (CODE) using global distributed ground-based GNSS receivers. The solar zenith angles are shown with yellow and black lines (where yellow lines correspond to the daytime and the thick white line is the solar terminator), while the orbit of Swarm A is presented as a magenta segment with timestamps annotated. Swarm A flew at around 22 local time; thus, we can expect local ionospheric disturbances in plasma density both at low and high latitudes. The plasma density is enhanced during daytime, and the noon is above Americas (cf. Figure 2a).

Figure 2b shows the raw electron density (*Ne*), background electron density (*bNe*), and electron temperature (*Te*) measured by Swarm A. The background electron density is derived as the 35th percentile in a running window of about 2,000 km in length (Jin, Spicher, et al., 2019). Low background density and enhanced electron temperatures correspond to the polar regions, while high background density and low temperatures are characteristics for the low-latitude region. There are strong variations in the electron density in the postsunset ionosphere at low latitudes, where we observe both plasma bubbles and plasma blobs (annotated with red and black arrows, respectively). We also observe strong local enhancement in the ionospheric density in the polar region at the end of the pass, being stronger when Swarm A was closer to the noon side at the southern high latitudes. We associate these enhancements with the polar cap patches (annotated with magenta arrows), which are strongest close to the dayside polar cap and gradually diminish during their convection over the polar cap (Carlson, 2012; Hosokawa et al., 2011). This pass confirms that Swarm can detect plasma variations and the corresponding structures along its orbit and can also relate them to the background density. To relate the measurements to different ionospheric regions, we make use of the field-aligned currents, which are shown in Figure 2c as measured from a single spacecraft (black line) and dual spacecraft (A and C, blue line). We consequently derive the auroral boundaries from FAC data of Swarm (Xiong & Lühr, 2014) and shade the auroral regions in light green.

During this pass, Swarm encountered various density structures. In the northern polar cap (poleward of the auroral region, i.e., 16:39–16:42 UT), plasma environment was quiet with no polar cap patches and with small density fluctuations. There was significantly enhanced electron temperature due to auroral particle precipitation. The auroral particle precipitation has also led to slight enhancements in the electron density there. From 16:56 to 17:03 UT, there was a series of plasma density depletions, which we associate with plasma bubbles. We also note that the first depletion appeared at midlatitudes (40° magnetic latitude (MLAT)) instead of the equatorial area (see Aa et al., 2018). This localized plasma depletion is more likely due to local plasma processes instead of plasma bubbles. One plasma blob was observed around 17:05 UT
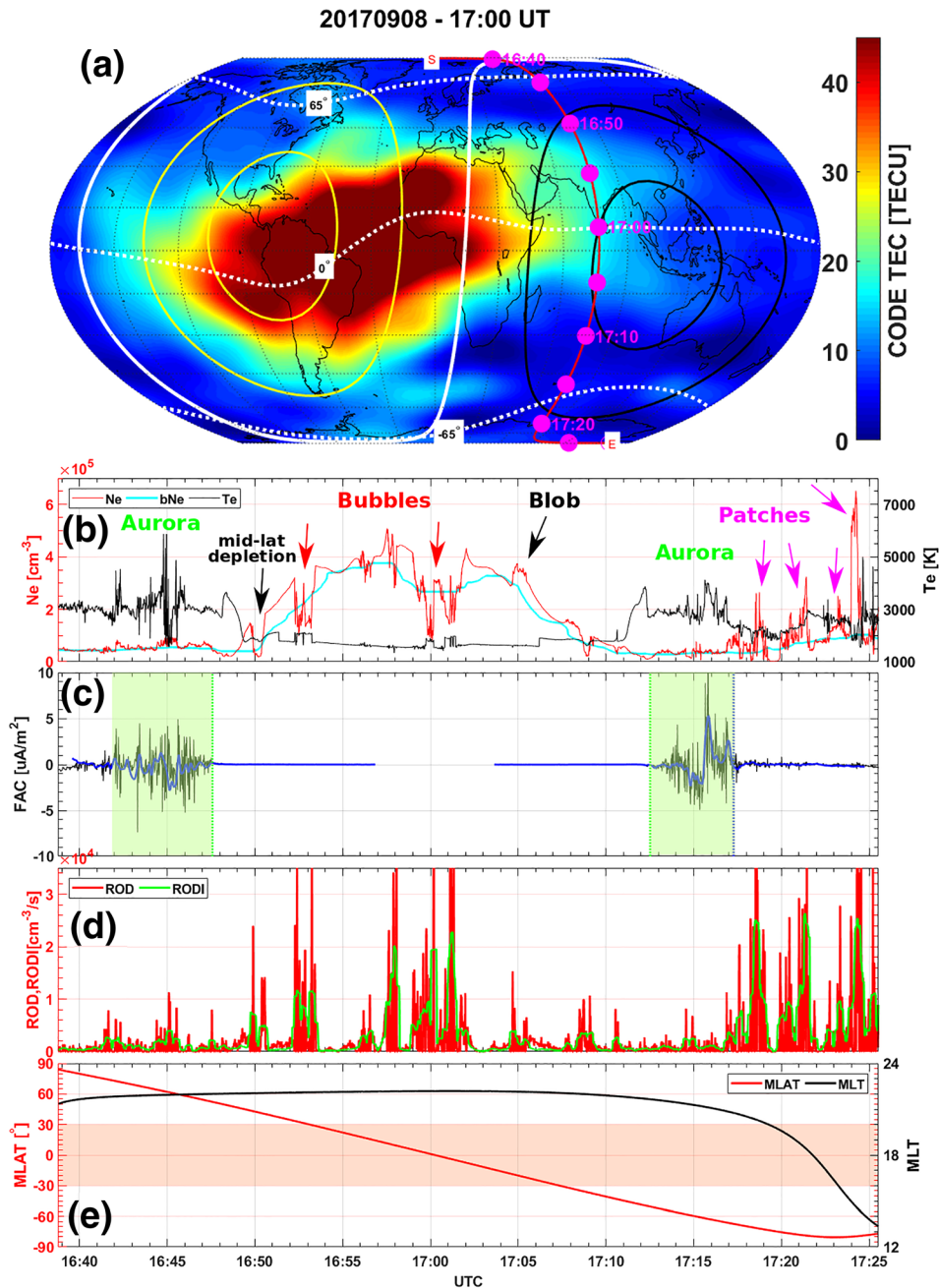
Figure 2. Observations by Swarm A during one pass from the north toward and over the South Pole. (a) The ground-based GIM from CODE. Magnetic equator and ±65° MLAT are displayed as white dotted lines. Black and yellow solid lines correspond to the solar zenith angles, and the white line presents the solar terminator. The orbit of Swarm A is shown as a magenta line with timestamps annotated. (b) The electron density (unfiltered, red), background electron density (*bNe*, cyan), and electron temperature (*Te*, black). (c) The field-aligned current (FAC) from the single spacecraft (black) and dual spacecraft (Swarm A and C, blue). The auroral region derived from the FAC dataset is shaded in green. (d) The derived irregularity parameter ROD in absolute values (red) and RODI (green). (e) The MLAT and MLT of the Swarm satellite. GIM = global ionosphere map; CODE = Center for Orbit Determination in Europe; FAC = field-aligned current; ROD = rate of change of density; RODI = rate of change of density index; MLAT = magnetic latitude; MLT = magnetic local time.

manifesting as an enhanced density structure above the background density. In the southern polar cap, several polar cap patches associated with significantly enhanced density were observed.

All these dynamical plasma structures associated with the low-latitude plasma bubbles or blobs, polar cap patches, and particle precipitation were characterized with density fluctuations. The fluctuations can be quantified by ROD and RODI as shown in Figure 2d (for ROD we show the absolute values). ROD and
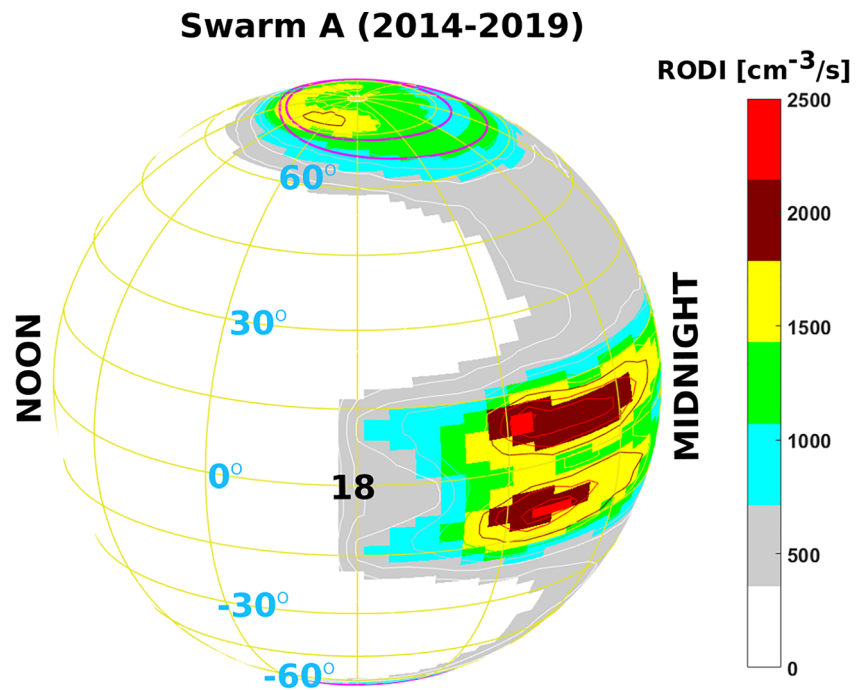
Figure 3. Global distribution of RODI in MLAT/MLT coordinates. The Sun is to the left (12 MLT), and the globe is shifted toward the northern hemisphere to show the northern polar area. A movie can be found in the supporting information that presents RODI at other latitudes and local times. The magenta curves are the poleward and equatorward boundaries of the auroral oval from the Feldstein model ($Q = 3$). MLAT = magnetic latitude; MLT = magnetic local time.

RODI show the largest variations associated with the plasma bubbles and polar cap patches—the phenomena that can lead to large plasma structuring (e.g., Moen et al., 2013; Xiong et al., 2010). RODI is a measure for the absolute fluctuations in the electron density, down to scales of ca. 7.5 km for good-quality data, as it is based on 2 Hz Swarm data, and it reflects plasma structuring due to different ionospheric phenomena without differentiating them. RODI can be used as a proxy for a global measure of ionospheric irregularities also in relation to the ionospheric scintillations, according to the scintillation models.

For completeness, we show in Figure 2e the MLAT and magnetic local time (MLT) of the Swarm satellite corresponding to this half orbit. The region within $\pm30°$ MLAT is shaded in pink. Note that for studying ionospheric irregularities in the literature, different thresholds have been used for calculating the occurrence probability (e.g., Kil & Heelis, 1998; Su et al., 2006; Xiong et al., 2010). However, in the following sections, we use the averaged RODI at a certain location for representing the irregularity intensity.

3.2. Global Distribution in Magnetic Coordinates

Since RODI can effectively reflect plasma irregularities along the Swarm orbit, we carry out large statistics to study the climatology of ionospheric plasma irregularities in years 2014–2019. Figure 3 shows the global distribution of RODI as a function of MLAT and MLT for the whole period of study. The data are binned into 2° in MLAT and 20 min in MLT. Here, we use the quasi-dipole magnetic coordinates (Emmert et al., 2010; Richmond, 1995). We noted data anomalies in the raw electron density data from the Swarm satellites, which affect the detection of ionospheric irregularities on the dayside at middle and low latitudes. The data anomalies in the Swarm data appear as artifacts at the solar zenith of ca. 50°, occur around 9 and 15 local time, and are likely connected to the orientation of spacecraft with respect to the Sun. They are not related to ionospheric irregularities, and as we did not find a systematic way to remove these artifacts, we choose to remove data between 7 and 17 MLT within $\pm30°$ MLAT when plotting Figure 3. For more details about these artifacts in the Swarm data, see the supporting information.
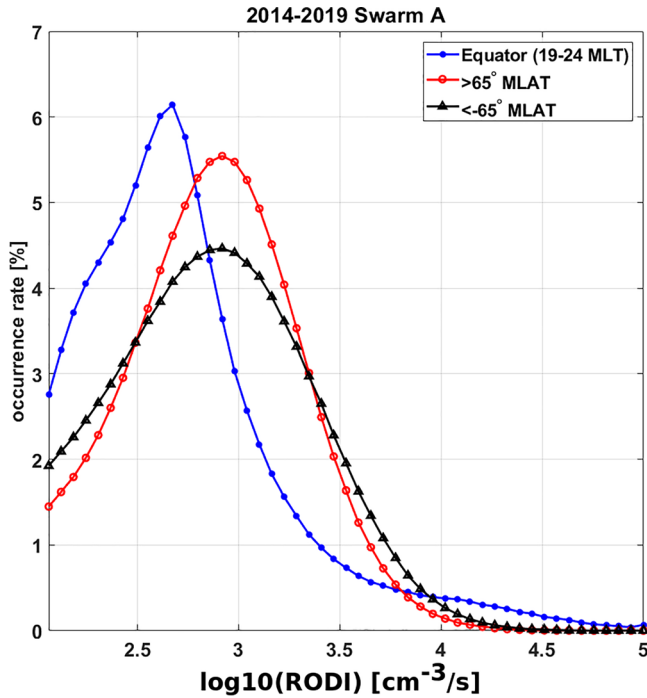
Figure 4. The occurrence rate of RODI at three different ionospheric regions: north polar ionosphere (>65° MLAT, red), south polar ionosphere (<−65° MLAT, black), and the nighttime equatorial ionosphere (−20° to 20° MLAT and 19 to 24 MLT, blue). Note that RODI is presented in a logarithmic scale. MLAT = magnetic latitude; MLT = magnetic local time.

In Figure 3, magnetic noon is on the left side. The general pattern of the irregularity distribution is strikingly similar to the global characteristics of ionospheric scintillations as summarized in Figure 1. RODI is enhanced around the magnetic equator in the postsunset sector. The Feldstein auroral oval is presented as magenta curves around the North Pole, and the high-latitude irregularities are distributed around the dayside cusp and at nightside auroral oval, as well as in the polar cap. However, one needs to keep in mind that the study by Basu, Mackenzie, and Basu (1988) has been carried out with only five ground-based receivers, and focusing on very high frequency (VHF) scintillations (using signals from 137 to 250 MHz), which are affected by kilometer-scale irregularities (Fresnel scale of 1.3–0.9 km). Due to data resolution of the Swarm instruments and orbital velocity, Swarm detects plasma irregularities that are at larger scales (>7.5 km) than those relevant to the study by Basu, Mackenzie, and Basu (1988). However, if we assume a turbulence cascading from large to small scales, irregularities detected by Swarm can also lead to smaller-scale irregularities, which are responsible for scintillations measured on the ground. An important aspect of our result is that it is the first in situ study of global distribution of ionospheric irregularities. The advantage of the Swarm satellites is that they provide both the high-resolution density data along the polar orbit and a long-term data set during a declining solar cycle, allowing for a climatology study, which will be presented in the following.

Since Figure 3 shows the in situ observation-based climatological map of global ionospheric irregularities created from direct measurements of plasma density along the whole satellite orbit, there are plenty of details in addition to the cartoon in Figure 1. Examples of such details are the exact locations of high intensity areas in terms of MLAT/MLT as well as the relative intensity and distribution of plasma irregularities at different latitudes. In addition, the dependence on the solar activity and the upstream solar wind can be investigated.

At low latitudes, ionospheric irregularities are located at two bands of latitudes that straddle the magnetic equator (i.e., between 0° and ±20° MLAT). RODI peaks around 21 MLT and remains high until midnight. The high-latitude irregularities are enhanced from the dayside cusp (~75° MLAT) and decay slowly toward the nightside polar cap. There are also sporadic enhancements in the nightside auroral oval.

In Figure 3, we only present the mean RODI at different latitudes. To study in more detail the differences in the distributions at different latitudes, we present the occurrence rate of different RODI values around the magnetic equator as well as in the Arctic and Antarctic in Figure 4. Note that here we use data only from 19 to 24 MLT around the magnetic equator where the plasma irregularities are the strongest, while for high latitudes, we use data poleward of ±65° MLAT at all MLTs. Due to large variations in RODI, we choose a logarithmic scale to present the distributions. It is obvious that the equatorial ionosphere shows a different aspect of distribution where most of RODI is at low values and peaks around 2.67 (RODI ~468 cm^{-3}/s). In the Arctic and Antarctic, RODI shows a similar distribution function that peaks around 2.9 (RODI ~813 cm^{-3}/s). In the Arctic, RODI has a larger population at lower values, and the probability of Antarctic RODI surpasses the Arctic one from about 3.4 (RODI ~2,559 cm^{-3}/s); that is, there are more extreme RODI values in the Antarctic compared to the Arctic. This can explain why there are more losses of GPS signal lock for the Swarm onboard receivers in the Antarctic (e.g., Xiong et al., 2016, 2018). By comparing the high and low latitudes, it is concluded that in the equatorial ionosphere there is a higher probability of more extreme values (large RODI) than at high latitudes. On the other hand, low latitudes also include a large population of small values. By checking the Swarm data orbit by orbit, we find that the low-latitude plasma structures such as bubbles and blobs are not often observed, while the high-latitude ionosphere is always associated with observable plasma fluctuations. This is due to the much easier and direct access of
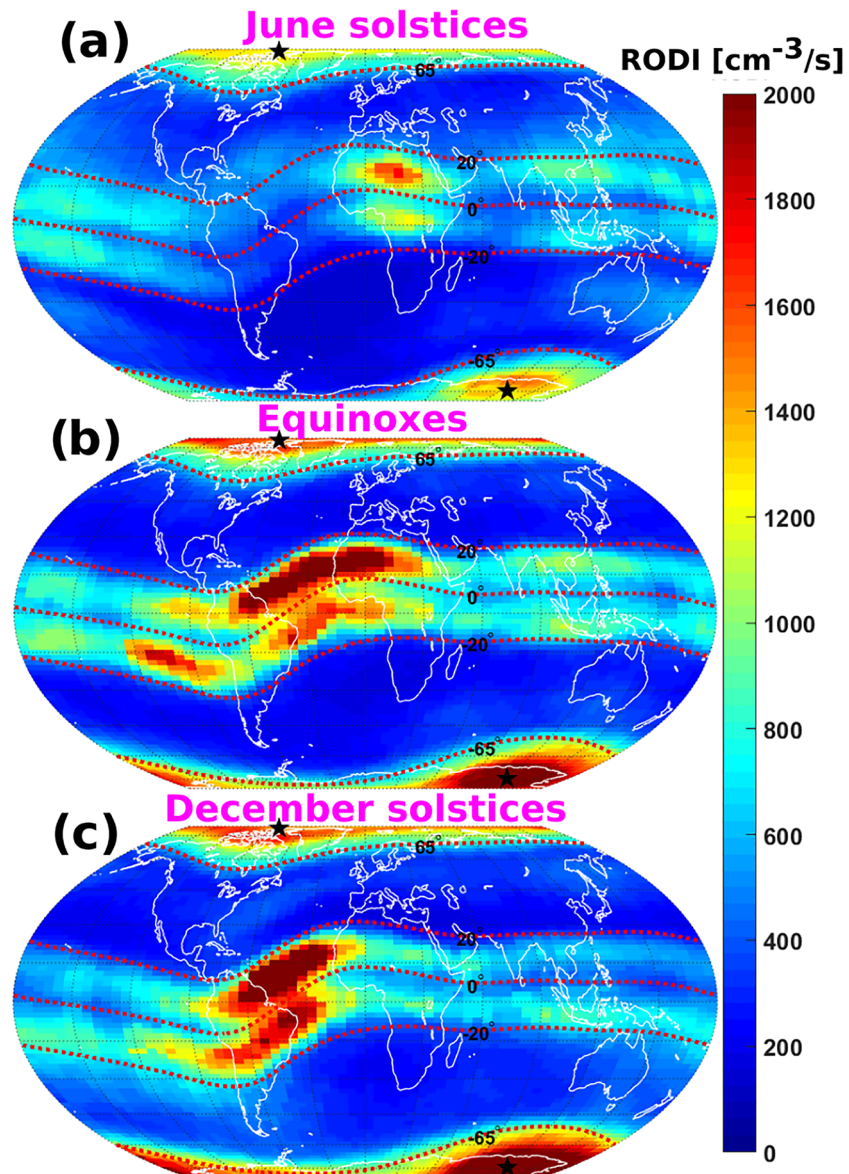
Figure 5. The global distribution of RODI for three different seasons in geographic coordinates. The magnetic latitudes of 0°, ±20°, and ±65° are plotted as magenta dotted lines. The geomagnetic poles in the northern and southern hemispheres are presented as black stars. Seasonal and longitudinal variations are observed at low latitudes.

energy input from the solar wind and magnetosphere (e.g., particle precipitations) into the ionosphere at high latitudes, where the ionosphere is structured even at a low level of plasma density. However, due to much lower background electron density, extreme events at high latitudes are much less frequent than those at low latitudes.

3.3. Geographic Distribution of Ionospheric Irregularities

After presenting the climatology of irregularities in magnetic coordinates, we proceed with the distribution in geographic coordinates. Figure 5 displays the global distribution of RODI in geographic coordinates. The RODI data are divided into bins of 2° in geographic latitude and 5° in geographic longitude using the Swarm data from April 2014 to April 2019. The longitudinal dependence of ionospheric irregularities at low latitudes is often reported to vary with seasons (Burke et al., 2004; Stolle et al., 2006). To demonstrate the seasonal effect, we divide the Swarm data into three seasons (June solstices, equinoxes, and December solstices). To construct the statistics of June and December solstices, the data are averaged over 131 days

around each solstice from April 2014 to April 2019, while the data are averaged over 65 days around March and September equinoxes for the Equinox season. In this way, we account for the slow precession of the Swarm orbit such that it takes ~131 days for Swarm to cover all local time sectors.

It is clear that regions of enhanced ionospheric irregularities are located on both sides of the magnetic equator (magenta line with 0° annotation) and around both poles poleward of $\pm65°$ MLAT for all seasons. Ionospheric irregularities are weaker between $\pm20°$ MLAT and $\pm65°$ MLAT. At high latitudes, the irregularity intensity shows interhemispheric asymmetry, and the irregularities also depend on longitude. Ionospheric irregularities are more pronounced in the Antarctic than in the Arctic. In the Arctic, RODI is higher over North Canada, while in the Antarctic, RODI is higher over longitudes 90–180°E. This confirms that the ionosphere and ionospheric irregularities are modulated by the Earth's magnetic field (Jin & Xiong, 2020). The locations of the north and south geomagnetic poles are presented as black stars in Figure 5. For more details about the high-latitude ionospheric irregularities, the readers are referred to study by Jin, Spicher, et al. (2019).

We try to extract information about the seasonal and longitudinal variations of low-latitude irregularities. Around June solstices, the most intense irregularities are over Africa on both sides of the magnetic equator. Moderate RODI values are also visible in other longitudes around 180–120°W and around 90–130°E (South Asia). Around equinoxes, the equatorial irregularities are significantly enhanced. In addition, the areas of high RODI values are larger. In this case, RODI is large in the region extending from South America to West Africa. There is also a clear interhemispheric asymmetry for this season; that is, RODI is higher in the northern hemisphere between longitudes 70°W and 30°E, while RODI in the southern hemisphere is higher between longitudes 120°W and 70°W.

Around December solstices, equatorial ionospheric irregularities are more confined over South America and over the South Atlantic region. Note that during June solstices and equinoxes, irregularities are stronger in the northern hemisphere than in the southern hemisphere. However, it is during December solstices that ionospheric irregularities in the southern hemisphere are becoming comparable to the northern hemisphere, and for certain longitudes, RODI is more enhanced in the southern hemisphere.

Regarding the seasonal and longitudinal variations, high-latitude irregularities show quite different features than the low-latitude ones. The locations of enhanced RODI in the Arctic and Antarctic are fairly constant around the geomagnetic poles (black stars in Figure 5). The only difference is the intensity of RODI during different seasons; that is, RODI is the weakest during June solstices, and it is significantly enhanced around equinoxes and December solstices. It is interesting to note that though the equatorial RODI during June solstices and equinoxes in the southern hemisphere is weaker than the northern hemisphere, RODI in the Antarctic during these seasons is higher than in the Arctic. This adds more complexity to the global picture, when comparing the interhemispheric irregularities without separating them by latitudes.

3.4. The Long-Term Variations of Ionospheric Irregularities

The Swarm satellites were launched in November 2013, and therefore, it is possible to study the long-term variations of ionospheric irregularities, for example, the characteristics of irregularities during different solar activities. Figure 6 gives an overview of the data from December 2013 to October 2019. Figure 6a shows the solar flux index P10.7 as an indication of the solar activity, where P10.7 = (F10.7 + F10.7A)/2, and F10.7A is the average of the F10.7 solar flux index in a running window of 81 days. The P10.7 index shows a decreasing solar irradiation, which is an indication of the declining phase of the current solar cycle. P10.7 decreased from around 150 sfu in 2014 to around 100 sfu in 2016, and then P10.7 is becoming very low and stable reaching around 60 sfu in 2019. Figure 6b shows the daily averaged electron density as a function of MLAT. To compensate for the effects due to the slowly varying orbit of Swarm, we have averaged the data using a running window of 131 days. Therefore, it is only possible to resolve temporal variations of duration longer than 131 days (~4 months). This is because Swarm uses 131 days to cover all local times. The density is obviously high at low latitudes as compared to the high latitudes. The two peaks of high density around $\pm10°$ MLAT are related to the equatorial ionization anomaly (EIA), with a trough near magnetic equator. The solar cycle variations of the electron density are very clear at all latitudes; that is, there is high electron density before 2016 and significantly lower density after 2016. The EIA is generally high from September to March each year. Figure 6c shows daily averaged RODI as a function of MLAT. For the same reason as for Ne, RODI
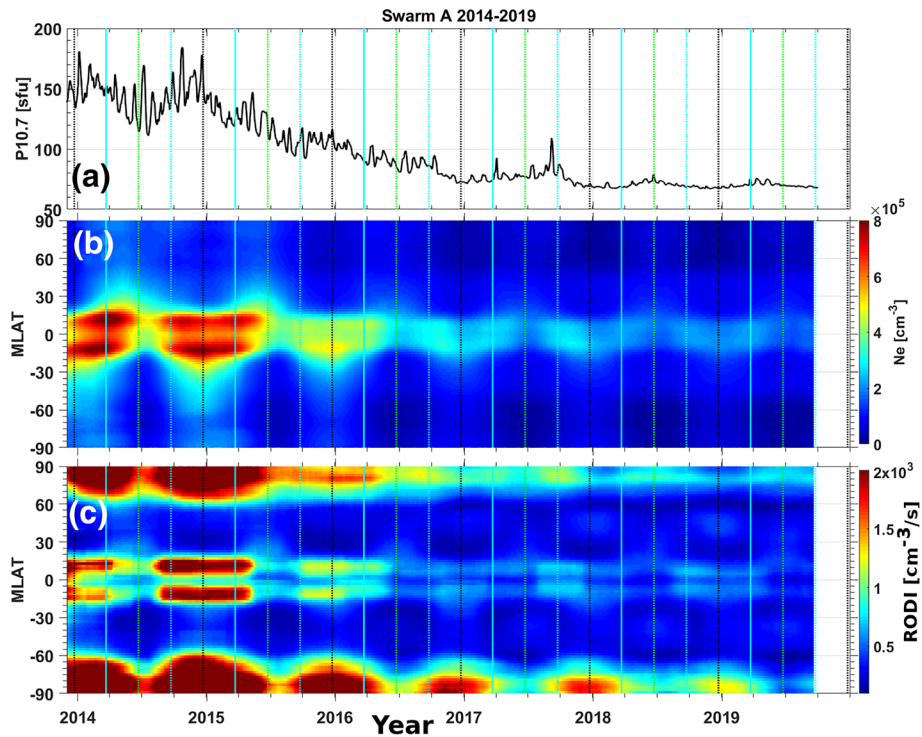
Figure 6. (a) The P10.7 index that is running averaged in 31 days. The long-term variations electron density (b) and RODI (c) as a function of day (November 2013 to September 2019) and MLAT. The vertical lines mark the equinoxes and solstices. The solar flux index P10.7 is given in the solar flux units (sfu), where $1\ \mathrm{sfu} = 10^{-22}\ \mathrm{W\ m^{-2}\ Hz^{-1}}$. MLAT = magnetic latitude.

is also running averaged over 131 days. On the contrary to the low electron density at high latitudes (poleward of $\pm 65°$ MLAT), RODI is highest at high latitudes. Significant RODI is also obvious near the EIA areas, but here the averaged RODI is lower in values and limited in areas. This is due to the different characteristics of ionospheric irregularities at different latitudes. At low latitudes, ionospheric irregularities tend to occur at certain local times (from postsunset to early morning) and at certain longitudes (South America to Africa). On the other hand, the high-latitude ionospheric irregularities can occur at any given local times and any longitudes. Furthermore, even during the most disturbed conditions (19–24 MLT), the majority of RODI is relatively low at low latitudes, while RODI at high latitudes is generally of moderate values (cf. Figure 4). This can explain higher averaged RODI values at high latitudes as compared to the low latitudes. There are also clear solar cycle variations with highest RODI values during high solar activity (before 2016) and low activity during the solar minimum (after 2016). Similar to the density in EIA, RODI during the solar maximum (2014–2016) is high from September to March at both high and low latitudes.

Finally, Figure 7 shows the yearly averaged electron density and RODI as a function of MLAT. For clarity, we only show data at low latitudes. The EIA is very clear with crests around $\pm 10°$ MLAT and a trough around $0°$ MLAT. As the solar activity becomes lower from 2014 to 2019, the electron density decreases dramatically. Furthermore, the locations of the ionization crests shift toward the magnetic equator accordingly. The latitudinal profiles of RODI also show two peaks near the crests of EIA. Similar to the EIA, RODI decreases dramatically, and the peak locations of RODI shift toward lower latitudes with the declining solar activity.

3.5. IMF Bz Dependence of Ionospheric Irregularities

The Earth's ionosphere is affected by the coupling between the upstream IMF and the Earth's magnetic field. For example, at high latitudes, the IMF Bz modulated magnetic reconnection affects ionospheric convection patterns and the formation of polar cap patches (Cowley & Lockwood, 1992; Lockwood & Carlson, 1992). At low latitudes, the IMF Bz affects the occurrence of plasma bubbles mainly by prompt penetration electric
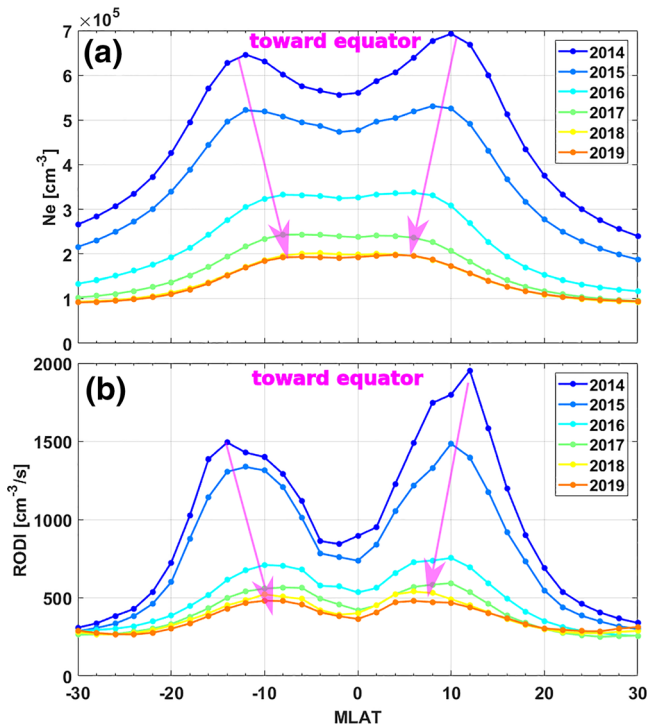
Figure 7. The distribution of electron density (a) and RODI (b) as a function of MLAT for different years. Both *Ne* and RODI are shifted toward lower magnetic latitudes during the declining phase of the current solar cycle.

field (e.g., Huang, 2011, and references therein). To test the impact of the IMF on global distribution of ionospheric irregularities, we divide the Swarm data according to the intensity of IMF *Bz*, which is taken from the 5 min averaged OMNI data set (King & Papitashvili, 2005). We smooth the IMF data using a moving average over 30 min before binning the Swarm data (Jin, Spicher, et al., 2019). Figure 8 presents the averaged RODI at high and low latitudes for *Bz* positive (left panels) and *Bz* negative (right panels). To avoid the ambiguity around $Bz = 0$ nT during the averaging process, we choose to present the cases for $Bz > 3$ nT and $Bz < -3$ nT as positive and negative *Bz* by considering both significant IMF polarity and the number of data points.

In Figures 8a–8d, we also plot the Feldstein auroral oval as solid magenta curves for reference (Holzworth & Meng, 1975). Figures 8a–8d clearly demonstrate the impact of IMF *Bz* on the distribution of ionospheric irregularities at high latitudes in both hemispheres. When *Bz* is positive, the region of intense irregularities is distributed at higher latitudes than for the negative *Bz* condition. For example, the dayside irregularities (6–12 MLT) are concentrated poleward of ±75° MLAT for *Bz* positive, while the daytime irregularities extend to regions equatorward of ±70° MLAT. This is also the case for the nightside irregularities; that is, ionospheric irregularities are well confined inside the polar cap and within the Feldstein auroral oval for *Bz* positive, while the region of intense irregularities extends to much lower latitudes for negative *Bz*.

One interesting topic concerns the interhemispheric asymmetry of ionospheric irregularities (Jin & Xiong, 2020). Comparison of Figures 8b and 8d shows that ionospheric irregularities are more enhanced in the southern central polar cap region and toward the dayside cusp in the northern hemisphere. At high latitudes, polar cap patches and their associated deformation are associated with the most significant plasma irregularities due to their high absolute density. One often observes very high-density polar cap patches in the southern hemisphere as shown in the example in Figure 2 (which is probably due to the large offset of the geomagnetic pole). As a result, the anti-sunward propagation of polar cap patches is better captured in the southern hemisphere than in the northern hemisphere. Therefore, we observe more enhanced irregularities in the southern central polar cap region. This also explains the clearer difference for negative IMF *Bz* when polar cap patches are the dominant phenomenon in the polar cap.

The division of ionospheric irregularities at low latitudes by IMF *Bz* also gives very interesting result. Figures 8e and 8f display the mean RODI during positive and negative IMF *Bz*, respectively. For *Bz* positive condition, ionospheric irregularities start to grow at ~19 MLT and remain significant until 2 MLT. There is also sporadically enhanced RODI around 4 MLT. For *Bz* negative, the MLT range of enhanced irregularities is more concentrated; that is, irregularities increase sharply around 19:30 MLT and decay very quickly around 23 MLT. In addition, the intensity of irregularities for *Bz* negative is also stronger than for *Bz* positive. This indicates that the development and maintenance of equatorial irregularities are more confined in MLT during negative *Bz*, while the occurrence of irregularities is more sporadic and extended during positive *Bz*.

4. Discussion

In this study, we have presented the first climatology of ionospheric irregularities at all latitudes using long-term observations from the Swarm in situ data (2014–2019). The climatology identifies three main regions of enhanced irregularities, that is, magnetic equator from sunset to early morning, along the auroral oval and inside the polar caps (cf. Figure 3).

At low latitudes, there are two peaks of ionospheric irregularities around ±10° MLAT (corresponding to the magnetic field line with apex height of ~662 km) and a trough at the magnetic equator. The irregularities increase quickly from 19:30 to 20:30 MLT, with a plateau until 23 MLT followed by a slow decrease until
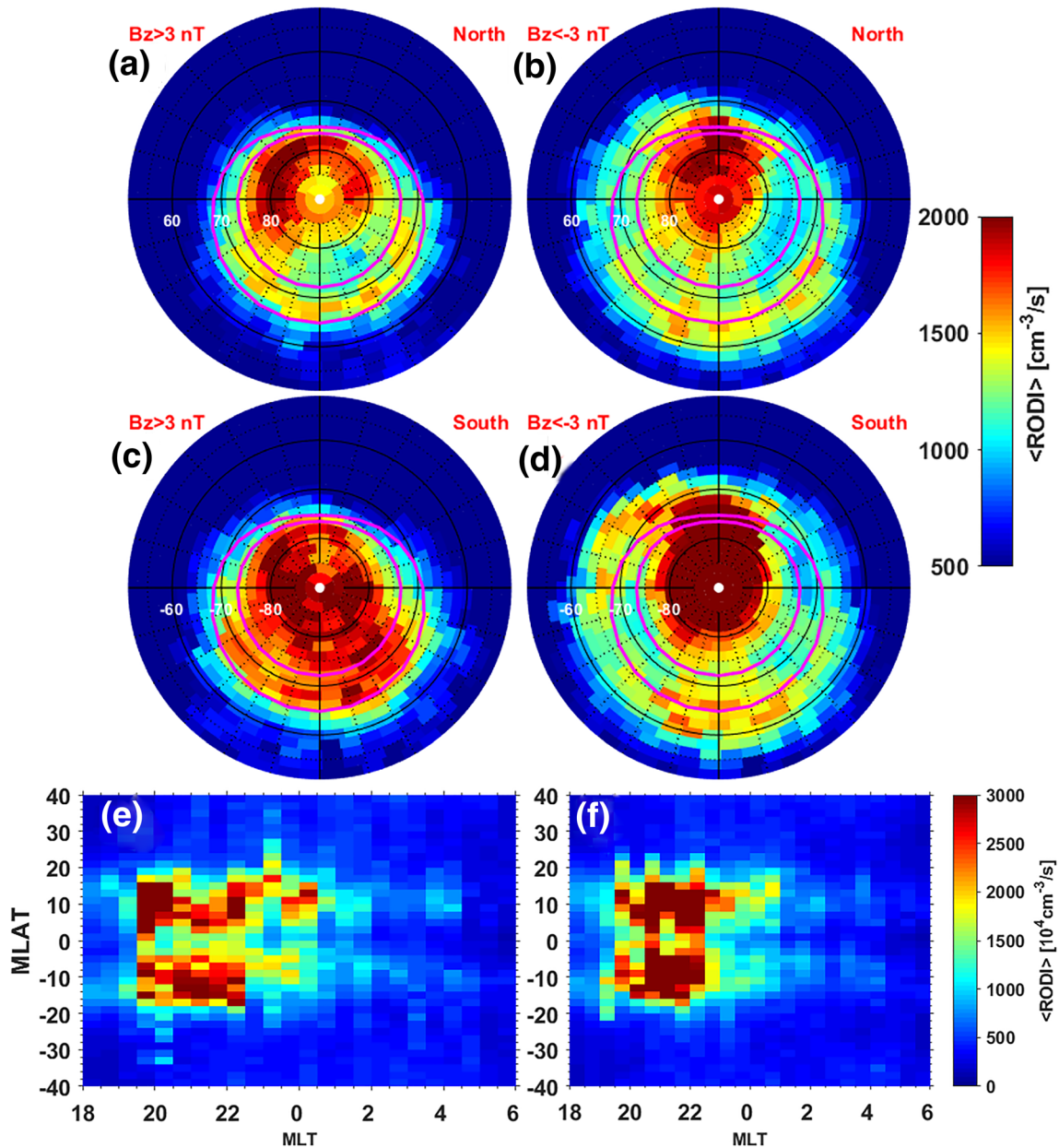
Figure 8. The IMF *Bz* dependence of the averaged RODI at high and low latitudes. (a–d) The distribution of mean RODI in a polar dial plot of MLAT/MLT coordinates at high latitudes. The Swarm data are binned in equal-area cells (Jin, Spicher, et al., 2019). (e, f) Mean RODI at low latitudes in MLAT/MLT coordinates. The Swarm data are divided in bins of 2° MLAT and 0.5 hr MLT.

early morning. In the global perspective, the high-latitude irregularities are always characterized by a moderate level of fluctuations, while the equatorial ionosphere is occupied by both low and very high levels of density fluctuations.

Ionospheric irregularities show strong dependence on solar activity. As the solar activity decreases from 2014 to 2019, the intensity of irregularities decreases significantly. Beside the variations of the irregularity intensity, the locations of ionospheric irregularities show slight difference as well. The latitudes of peak RODI shift toward the magnetic equator from around ±12° MLAT in 2014 to around ±6° MLAT in 2019. This feature is similar to previous studies of the equatorial plasma bubbles observed by CHAMP and GRACE missions at different solar activity conditions (e.g., Xiong et al., 2010). The occurrence of postsunset equatorial plasma bubbles is closely related to the vertical plasma drift (e.g., Stolle et al., 2008; Su et al., 2008), and it

has been reported that the strength of pre-reversal enhancement of eastward electric field around sunset hours decreases significantly from the solar maximum to solar minimum (Fejer et al., 1995). As a result, the plasma bubbles at low solar activity do not reach as high altitude as those in the solar maximum period (Nishioka et al., 2008). The apex height of MLAT can be converted from the following formula:

$$Apex\ height = (L - 1) \cdot Re$$

$$Where\ L = \frac{r}{Re} \frac{1}{\cos^2 MLAT}$$

where r is the radial distance of the measurement point from the Earth center and Re = 6,371.2 km is the mean value of Earth's radius (Lühr & Xiong, 2010). The peak occurrence of ionospheric irregularities shifts from 12° MLAT (high solar activity) to 6° MLAT (low solar activity) suggesting that the mean apex height of equatorial plasma bubbles changes from 758 to 525 km for different levels of solar activity.

We would like to mention that the Swarm satellites fly close to the peak height of the F2 layer (mostly above the F2 peak); therefore, the plasma density irregularities observed by Swarm should reflect well the ground-based ionospheric scintillations because the irregularities close to F2 layer contribute most to the ground scintillation data (Aarons, 1993). RODI is enhanced around the magnetic equator in the postsunset sector, and the high-latitude irregularities are distributed around the dayside cusp and at nightside auroral oval, as well as in the polar cap. The similarity of the statistics of in situ measurements of plasma irregularities and the ground-based measurements of scintillations is encouraging (cf. Figures 1 and 3).

However, one should not expect a perfect relationship between the ground-based scintillation measurements and ionospheric irregularities detected in this present study. Swarm satellites fly at an altitude of ~450 km, which is slightly higher than the typical ionosphere peak height (350–400 km). Scintillations are an integrated effect along the ray path from a receiver on ground to a satellite. At high latitudes, the relation between scintillation data and in situ electron density data should be good since the magnetic field is almost perpendicular to the satellite orbit and the plasma structures are parallel to the magnetic field (field-aligned irregularities). Therefore, the Swarm in situ data can be mapped down to the peak height of the ionosphere. However, the situation is not straightforward at low latitudes due to the parallel configuration of the magnetic field. There are two categories of ionospheric irregularities, that is, a thin layer of irregularities at the bottomside (200–400 km) or layers not fully extended in altitude and plume-like irregularities extended in altitude (Aarons, 1993). A thin layer of irregularities that is below the altitude of Swarm cannot be detected by the in situ measurements. However, this layer of irregularities affects the ground scintillation as long as the ray path intersect with it. Surely, a thin layer of irregularities usually causes less effect on satellite signals. In other words, the irregularities detected by Swarm should affect ground scintillations if the ray path intersects with the orbit of Swarm, while the ground scintillations may not necessarily imply in situ detection of irregularities by Swarm.

In addition to the arguments presented before, there is another reason that prevents the direct link of irregularities by in situ technique and ground scintillations; that is, they are sensitive to irregularities at different scales. Due to the growing number of GNSS-based applications in our society, there is an increasing concern about ionospheric scintillations at GNSS frequencies. The spatial scales of irregularities that affect GNSS amplitude scintillations are ~400 m (Fresnel radius). Unfortunately, Swarm does not resolve irregularities at such scales. Since the Swarm Langmuir probe data have a resolution of 2 Hz, the gradients can be resolved down to ~7.5 km. It is not straightforward to use the phase screen theory to predict amplitude scintillations on the ground (Basu, Basu, et al., 1988; Rino, 1979). However, it is anticipated that the global climatology of ionospheric scintillation should be similar to the Swarm in situ observations due to turbulent energy cascading of irregularities from large scales to smaller scales (e.g., Basu et al., 1978). A close comparison of Figure 3 with the cartoon in Figure 1 suggests this relationship. The climatology of ionospheric irregularities presented in this study also agrees with the loss of lock of GPS receiver onboard Swarm satellites (Buchert et al., 2015; Xiong et al., 2018). For a more direct comparison of in situ plasma density data with ground-based scintillations, we will need high-resolution plasma data (e.g., Jin, Moen, et al., 2019). One can also conduct a large statistical study of ground-based ionospheric scintillations to verify the agreement with the climatology of in situ measurements.

To study how the upstream IMF affects the global distribution of ionospheric irregularities, we divided the Swarm data by the polarity of the IMF Bz. At high latitudes, the IMF Bz clearly controls the latitudes of irregularity occurrence. For positive Bz, the auroral oval and convection cells are smaller compared to the scenario of negative Bz. As a result, the regions of intense irregularities are confined to very high latitudes. In addition, the polar cap arcs are very common during positive Bz (Carlson, 2012). The structured particle precipitations from polar cap arcs can create detectable irregularities by the Swarm satellites. For Bz negative, the dayside magnetic reconnection erodes the closed magnetic field and causes the expansion of the auroral oval and polar cap. Polar cap patches are expected to form by transporting the high-density plasma from the dayside sunlit ionosphere. Significant irregularities are associated with polar cap patches (Jin et al., 2014; Mitchell et al., 2005). This explains the expansion of intense irregularities to lower latitudes during negative Bz.

For the first time, we statistically investigate the Swarm data at low latitudes according to the upstream IMF Bz. The interplanetary electric field associated with southward IMF Bz penetrates to the equatorial ionosphere. It induces eastward electric field on the dayside and westward electric field on the nightside (Kelley, 2009). Numerical simulations indicate that the reversal from eastward and westward electric field is around 22–23 MLT (Fejer et al., 1990; Huba et al., 2005). The eastward penetration electric field on the dusk side lifts the ionosphere upward and creates plasma bubbles. This is why we see more enhanced RODI during 20–23 MLT for Bz negative than Bz positive. The westward electric field in the post-midnight sector will suppress the creation of plasma bubbles. This effect is also reflected by more rapid decay of RODI during negative Bz than during positive Bz (cf. Figures 8e and 8f).

It is very interesting to note that RODI maximizes around 21 MLT at low latitudes (cf. Figure 3 and Figures 8e and 8f). However, in this study we are using the in situ data from the Swarm satellite, which is a polar orbiting satellite, and its local time is relatively fixed in couple of days. This may result in some discrepancy when comparing with ground-based instruments if only 1 or 2 days of observations are being considered. Plasma bubbles are mainly developed just after sunset, that is, around 20 LT (Ajith et al., 2015). The plasma irregularities that are detected by Swarm may be developed elsewhere and drifted to the location of Swarm. However, this discrepancy can be largely reduced if a longer data set is used (as we did in this study). In addition, the occurrence peak of equatorial plasma irregularities appears slightly later during lower solar activity (22 LT) compared to about 21 LT during higher solar activity (see Figure 8 of Xiong et al., 2010). We believe that the global climatology of irregularities derived from Swarm shown in our study has provided good reference for the ground-based facilities as well as irregularity modeling.

5. Conclusion

Ionospheric irregularities are important space weather problems that can significantly affect high frequency communications and satellite-based navigational systems. Our modern society relies more and more on applications that are based on such systems. Thus, there is an increasing need for an extensive knowledge of ionospheric irregularities and their global extent. However, few systems are able to monitor the distribution and occurrences of ionospheric irregularities at all latitudes, longitudes, and local times. The polar orbiting Swarm mission provides an opportunity to study ionospheric irregularities globally.

In this study, we use the plasma irregularity index, that is, RODI derived from the 2 Hz in situ data from the Langmuir probes onboard Swarm, to address this issue. The climatological map of RODI in MLAT/MLT coordinates shows three main regions of strong ionospheric irregularities, that is, around the magnetic equator, in the auroral zone (from dayside cusp to nightside auroral oval) and in the polar caps. In the equatorial ionosphere, ionospheric irregularities form two bands of enhancement centered around $\pm10°$ magnetic latitude. Due to the closeness of the Swarm altitude to the ionospheric F2 peak, it is natural to relate in situ ionospheric irregularities to ionospheric scintillations experienced on the ground. The similarity between this climatology and previous summary of ground-based scintillations is encouraging. However, due to data resolution of Swarm, it is not straightforward to directly correlate irregularities observed by Swarm with the ground-based scintillation data.

For the first time, we directly compare the distribution of irregularities at high and low latitudes in terms of their intensity. The majority of the equatorial ionosphere is characterized by relative smooth variations (no fluctuations). However, the occurrence rate of high RODI values (strong irregularities) is significantly higher

at low latitudes than at high latitudes. This explains why more losses of signal lock are observed at low latitudes as compared to high latitudes (Xiong et al., 2018).

Ionospheric irregularities also clearly depend on longitudes, at both low and high latitudes. At high latitudes, ionospheric irregularities are more enhanced near regions close to the geomagnetic poles. The equatorial irregularities, on the other hand, display interesting seasonal and longitudinal variations; that is, they are most prominent over South America during the December solstice, and they are located over Africa during the June solstice.

By using nearly 6 years of Swarm data, we present the long-term variations of ionospheric irregularities. Beside the seasonal variations, the magnitude of ionospheric irregularities at all latitudes is strongly controlled by the solar activity. With the declining solar activity, ionospheric irregularities become significantly weaker after 2016 than before.

Through different mechanisms, the upstream IMF is known to affect the creation of polar cap patches at high latitudes and plasma bubbles at low latitudes. As a preliminary test, we examined the impact of the upstream IMF Bz on the distribution of ionospheric irregularities. As expected, the IMF Bz modulates the occurrence of ionospheric irregularities at both high and low latitudes. For Bz positive, ionospheric irregularities at high latitudes are more constrained at relatively high latitudes, while they extend to much lower latitudes for Bz negative. At low latitudes, ionospheric irregularities are weaker in intensity and more spread in MLT for Bz positive than those during negative Bz.

Together with other irregularity parameters in IPIR, Swarm provides a new possibility for investigating ionospheric irregularities and scintillations as well as insights into plasma instability processes. Due to the good spatial coverage (all latitudes and longitudes) of the Swarm data, the irregularity parameter used in this study has an advantage in the ionospheric interhemispheric and inter-latitudinal studies. This study has important implications for a more realistic modeling of ionospheric scintillations both in their global extent and in their intensities.

Data Availability Statement

The Swarm data can be obtained through the official Swarm website (ftp://Swarm-diss.eo.esa.int). The CODE GIM data were obtained online (from ftp://ftp.aiub.unibe.ch/CODE/). The F10.7 index can be obtained from the GSFC/SPDF OMNIWeb interface (at https://omniweb.gsfc.nasa.gov). The IMF data are provided by the NASA OMNIWeb service (http://omniweb.gsfc.nasa.gov).

References

Aa, E., Huang, W., Liu, S., Ridley, A., Zou, S., Shi, L., et al. (2018). Midlatitude plasma bubbles over China and adjacent areas during a magnetic storm on 8 September 2017. *Space Weather-the International Journal of Research and Applications*, *16*(3), 321–331. https://doi.org/10.1002/2017SW001776

Aarons, J. (1993). The longitudinal morphology of equatorial F-layer irregularities relevant to their occurrence. *Space Science Reviews*, *63*(3–4), 209–243. https://doi.org/10.1007/bf00750769

Ajith, K. K., Ram, S. T., Yamamoto, M., Yokoyama, T., Gowtam, V. S., Otsuka, Y., et al. (2015). Explicit characteristics of evolutionary-type plasma bubbles observed from Equatorial Atmosphere Radar during the low to moderate solar activity years 2010–2012. *Journal of Geophysical Research: Space Physics*, *120*, 1371–1382. https://doi.org/10.1002/2014JA020878

Basu, S., Basu, S., Aarons, J., McClure, J. P., & Cousins, M. D. (1978). On the coexistence of kilometer- and meter-scale irregularities in the nighttime equatorial F region. *Journal of Geophysical Research*, *83*(A9), 4219–4226. https://doi.org/10.1029/JA083iA09p04219

Basu, S., Basu, S., Weber, E. J., & Coley, W. R. (1988). Case-study of polar-cap scintillation modeling using De-2 irregularity measurements at 800 km. *Radio Science*, *23*(4), 545–553. https://doi.org/10.1029/RS023i004p00545

Basu, S., & Groves, K. M. (2001). Specification and forecasting of outages on satellite communication and navigation systems. *Space Weather-the International Journal of Research and Applications*, *125*, 423–430. Retrieved from <go to ISI>://WOS:000277201400048

Basu, S., Mackenzie, E., & Basu, S. (1988). Ionospheric constraints on VHF/UHF communications links during solar maximum and minimum periods. *Radio Science*, *23*(3), 363–378. https://doi.org/10.1029/RS023i003p00363

Booker, H. G., Ratcliffe, J. A., & Shinn, D. H. (1950). Diffraction from an irregular screen with applications to ionospheric problems. *Philosophical Transactions of the Royal Society of London Series a-Mathematical and Physical Sciences*, *242*(856), 579–607. https://doi.org/10.1098/rsta.1950.0011

Buchert, S., Zangerl, F., Sust, M., Andre, M., Eriksson, A., Wahlund, J.-E., & Opgenoorth, H. (2015). SWARM observations of equatorial electron densities and topside GPS track losses. *Geophysical Research Letters*, *42*, 2088–2092. https://doi.org/10.1002/2015GL063121

Burke, W. J., Huang, C. Y., Gentile, L. C., & Bauer, L. (2004). Seasonal-longitudinal variability of equatorial plasma bubbles. *Annales Geophysicae*, *22*(9), 3089–3098. https://doi.org/10.5194/angeo-22-3089-2004

Carlson, H. C. (2012). Sharpening our thinking about polar cap ionospheric patch morphology, research, and mitigation techniques. *Radio Science*, *47*, RS0L21. https://doi.org/10.1029/2011RS004946

Cowley, S. W. H., & Lockwood, M. (1992). Excitation and decay of solar wind-driven flows in the magnetosphere-ionosphere system. *Annales Geophysicae-Atmospheres Hydrospheres and Space Sciences*, *10*(1–2), 103–115. Retrieved from <Go to ISI>://WOS: A1992HL02700010

Datta-Barua, S., Walter, T., Bust, G. S., & Wanner, W. (2014). Effects of solar cycle 24 activity on WAAS navigation. *Space Weather-the International Journal of Research and Applications*, *12*(1), 46–63. https://doi.org/10.1002/2013SW000982

Emmert, J. T., Richmond, A. D., & Drob, D. P. (2010). A computationally compact representation of Magnetic-Apex and Quasi-Dipole coordinates with smooth base vectors. *Journal of Geophysical Research*, *115*, A08322. https://doi.org/10.1029/2010JA015326

Farley, D. T., Balsey, B. B., Woodman, R. F., & McClure, J. P. (1970). Equatorial spread F: Implications of VHF radar observations. *Journal of Geophysical Research*, *75*(34), 7199–7216. https://doi.org/10.1029/JA075i034p07199

Fejer, B. G., Depaula, E. R., Heelis, R. A., & Hanson, W. B. (1995). Global equatorial ionospheric vertical plasma drifts measured by the AE-E satellite. *Journal of Geophysical Research*, *100*(A4), 5769–5776. https://doi.org/10.1029/94JA03240

Fejer, B. G., Spiro, R., Wolf, R., & Foster, J. (1990). Latitudinal variation of perturbation electric fields during magnetically disturbed periods-1986 Sundial observations and model results. Paper presented at the Annales Geophysicae.

Hey, J. S., Parsons, S. J., & Phillips, J. W. (1946). Fluctuations in cosmic radiation at radio-frequencies. *Nature*, *158*(4007), 234–234. https://doi.org/10.1038/158234a0

Hocke, K., Liu, H., Pedatella, N., & Ma, G. (2019). Global sounding of F region irregularities by COSMIC during a geomagnetic storm. *Annales de Geophysique*, *37*(2), 235–242. https://doi.org/10.5194/angeo-37-235-2019

Holzworth, R. H., & Meng, C. I. (1975). Mathematical representation of auroral oval. *Geophysical Research Letters*, *2*(9), 377–380. https://doi.org/10.1029/GL002i009p00377

Hosokawa, K., Moen, J. I., Shiokawa, K., & Otsuka, Y. (2011). Decay of polar cap patch. *Journal of Geophysical Research*, *116*, A05306. https://doi.org/10.1029/2010JA016297

Hosokawa, K., Otsuka, Y., Ogawa, Y., & Tsugawa, T. (2014). Observations of GPS scintillation during an isolated auroral substorm. *Progress in Earth and Planetary Science*, *1*(1), 16. https://doi.org/10.1186/2197-4284-1-16

Huang, C.-S. (2011). Occurrence of equatorial plasma bubbles during intense magnetic storms. *International Journal of Geophysics, 2011*.

Huang, C.-S., Le, G., de La Beaujardiere, O., Roddy, P. A., Hunton, D. E., Pfaff, R. F., & Hairston, M. R. (2014). Relationship between plasma bubbles and density enhancements: Observations and interpretation. *Journal of Geophysical Research: Space Physics*, *119*, 1325–1336. https://doi.org/10.1002/2013JA019579

Huba, J., Joyce, G., Sazykin, S., Wolf, R., & Spiro, R. (2005). Simulation study of penetration electric field effects on the low-to mid-latitude ionosphere. *Geophysical Research Letters*, *32*, L23101. https://doi.org/10.1029/2005GL024162

Jin, Y., Moen, J. I., Spicher, A., Oksavik, K., Miloch, W. J., Clausen, L. B. N., et al. (2019). Simultaneous rocket and scintillation observations of plasma irregularities associated with a reversed flow event in the cusp ionosphere. *Journal of Geophysical Research: Space Physics*, *124*, 7098–7111. https://doi.org/10.1029/2019JA026942

Jin, Y., & Xiong, C. (2020). Interhemispheric asymmetry of large-scale electron density gradients in the polar cap ionosphere: UT and seasonal variations. *Journal of Geophysical Research: Space Physics*, *125*, e2019JA027601. https://doi.org/10.1029/2019JA027601

Jin, Y. Q., Moen, J. I., & Miloch, W. J. (2014). GPS scintillation effects associated with polar cap patches and substorm auroral activity: Direct comparison. *Journal of Space Weather and Space Climate*, *4*(A23), A23. https://doi.org/10.1051/swsc/2014019

Jin, Y. Q., Moen, J. I., & Miloch, W. J. (2015). On the collocation of the cusp aurora and the GPS phase scintillation: A statistical study. *Journal of Geophysical Research: Space Physics*, *120*, 9176–9191. https://doi.org/10.1002/2015JA021449

Jin, Y. Q., Moen, J. I., Miloch, W. J., Clausen, L. B. N., & Oksavik, K. (2016). Statistical study of the GNSS phase scintillation associated with two types of auroral blobs. *Journal of Geophysical Research: Space Physics*, *121*, 4679–4697. https://doi.org/10.1002/2016JA022613

Jin, Y. Q., Moen, J. I., Oksavik, K., Spicher, A., Clausen, L. B. N., & Miloch, W. J. (2017). GPS scintillations associated with cusp dynamics and polar cap patches. *Journal of Space Weather and Space Climate*, *7*. https://doi.org/10.1051/swsc/2017022

Jin, Y. Q., Spicher, A., Xiong, C., Clausen, L. B. N., Kervalishvili, G., Stolle, C., & Miloch, W. J. (2019). Ionospheric plasma irregularities characterized by the Swarm satellites: Statistics at high latitudes. *Journal of Geophysical Research: Space Physics*, *124*, 1262–1282. https://doi.org/10.1029/2018JA026063

Kelley, M. C. (2009). *The Earth's ionosphere: Plasma physics and electrodynamics*. New York: Academic Press.

Kil, H., & Heelis, R. A. (1998). Global distribution of density irregularities in the equatorial ionosphere. *Journal of Geophysical Research*, *103*(A1), 407–417. https://doi.org/10.1029/97JA02698

Kil, H., Paxton, L. J., Jee, G., & Nikoukar, R. (2019). Plasma blobs associated with medium-scale traveling ionospheric disturbances. *Geophysical Research Letters*, *46*, 3575–3581. https://doi.org/10.1029/2019gl082026

King, J. H., & Papitashvili, N. E. (2005). Solar wind spatial scales in and comparisons of hourly Wind and ACE plasma and magnetic field data. *Journal of Geophysical Research*, *110*, A02104. https://doi.org/10.1029/2004JA010649

Kintner, P. M., & Ledvina, B. M. (2005). The ionosphere, radio navigation, and global navigation satellite systems. *Advances in Space Research*, *35*(5), 788–811. https://doi.org/10.1016/j.asr.2004.12.076

Kintner, P. M., Ledvina, B. M., & De Paula, E. R. (2007). GPS and ionospheric scintillations. *Space Weather-the International Journal of Research and Applications*, *5*(9). https://doi.org/10.1029/2006sw000260

Knudsen, D. J., Burchill, J. K., Buchert, S. C., Eriksson, A. I., Gill, R., Wahlund, J. E., et al. (2017). Thermal ion imagers and Langmuir probes in the Swarm electric field instruments. *Journal of Geophysical Research: Space Physics*, *122*, 2655–2673. https://doi.org/10.1002/2016JA022571

Ko, C. P., & Yeh, H. C. (2010). COSMIC/FORMOSAT-3 observations of equatorial F region irregularities in the SAA longitude sector. *Journal of Geophysical Research*, *115*, A11309. https://doi.org/10.1029/2010JA015618

Lockwood, M., & Carlson, H. C. (1992). Production of polar-cap electron-density patches by transient magnetopause reconnection. *Geophysical Research Letters*, *19*(17), 1731–1734. https://doi.org/10.1029/92GL01993

Lühr, H., Park, J., Gjerloev, J. W., Rauberg, J., Michaelis, I., Merayo, J. M. G., & Brauer, P. (2015). Field-aligned currents' scale analysis performed with the Swarm constellation. *Geophysical Research Letters*, *42*, 1–8. https://doi.org/10.1002/2014GL062453

Lühr, H., & Xiong, C. (2010). IRI-2007 model overestimates electron density during the 23/24 solar minimum. *Geophysical Research Letters*, *37*, L23101. https://doi.org/10.1029/2010GL045430

Mitchell, C. N., Alfonsi, L., De Franceschi, G., Lester, M., Romano, V., & Wernik, A. W. (2005). GPS TEC and scintillation measurements from the polar ionosphere during the October 2003 storm. *Geophysical Research Letters*, *32*, L12S03. https://doi.org/10.1029/2004GL021644

Moen, J., Oksavik, K., Alfonsi, L., Daabakk, Y., Romano, V., & Spogli, L. (2013). Space weather challenges of the polar cap ionosphere. *Journal of Space Weather and Space Climate*, *3*, A02. https://doi.org/10.1051/swsc/2013025

Nishioka, M., Saito, A., & Tsugawa, T. (2008). Occurrence characteristics of plasma bubble derived from global ground-based GPS receiver networks. *Journal of Geophysical Research*, *113*, A05301. https://doi.org/10.1029/2007JA012605

Oksavik, K., van der Meeren, C., Lorentzen, D. A., Baddeley, L. J., & Moen, J. (2015). Scintillation and loss of signal lock from poleward moving auroral forms in the cusp ionosphere. *Journal of Geophysical Research: Space Physics*, *120*, 9161–9175. https://doi.org/10.1002/2015JA021528

Olsen, N., Friis-Christensen, E., Floberghagen, R., Alken, P., Beggan, C. D., Chulliat, A., et al. (2013). The Swarm Satellite Constellation Application and Research Facility (SCARF) and Swarm data products. *Earth, Planets and Space*, *65*(11), 1189–1200. https://doi.org/10.5047/eps.2013.07.001

Park, J., Min, K. W., Lee, J. J., Kil, H., Kim, V. P., Kim, H. J., et al. (2003). Plasma blob events observed by KOMPSAT-1 and DMSP F15 in the low latitude nighttime upper ionosphere. *Geophysical Research Letters*, *30*(21), 2114. https://doi.org/10.1029/2003GL018249

Prikryl, P., Jayachandran, P. T., Chadwick, R., & Kelly, T. D. (2015). Climatology of GPS phase scintillation at northern high latitudes for the period from 2008 to 2013. *Annales Geophysicae*, *33*(5), 531–545. https://doi.org/10.5194/angeo-33-531-2015

Richmond, A. D. (1995). Ionospheric electrodynamics using magnetic apex coordinates. *Journal of Geomagnetism and Geoelectricity*, *47*(2), 191–212. https://doi.org/10.5636/jgg.47.191

Rino, C. L. (1979). Power law phase screen model for ionospheric scintillation.1. Weak scatter. *Radio Science*, *14*(6), 1135–1145. https://doi.org/10.1029/RS014i006p01135

Spicher, A., Cameron, T., Grono, E. M., Yakymenko, K. N., Buchert, S. C., Clausen, L. B. N., et al. (2015). Observation of polar cap patches and calculation of gradient drift instability growth times: A Swarm case study. *Geophysical Research Letters*, *42*, 201–206. https://doi.org/10.1002/2014GL062590

Spicher, A., Clausen, L. B. N., Miloch, W. J., Lofstad, V., Jin, Y., & Moen, J. I. (2017). Interhemispheric study of polar cap patch occurrence based on Swarm in situ data. *Journal of Geophysical Research: Space Physics*, *122*, 3837–3851. https://doi.org/10.1002/2016JA023750

Spogli, L., Alfonsi, L., Cilliers, P. J., Correia, E., De Franceschi, G., Mitchell, C. N., et al. (2013). GPS scintillations and total electron content climatology in the southern low, middle and high latitude regions. *Annals of Geophysics*, *56*(2). https://doi.org/10.4401/ag-6240

Spogli, L., Alfonsi, L., Romano, V., De Franceschi, G., Monico, J. F. G., Shimabukuro, M. H., et al. (2013). Assessing the GNSS scintillation climate over Brazil under increasing solar activity. *Journal of Atmospheric and Solar-Terrestrial Physics*, *105-106*, 199–206. https://doi.org/10.1016/j.jastp.2013.10.003

Stolle, C., Lühr, H., & Fejer, B. G. (2008). Relation between the occurrence rate of ESF and the equatorial vertical plasma drift velocity at sunset derived from global observations. *Annales Geophysicae*, *26*(12), 3979–3988. https://doi.org/10.5194/angeo-26-3979-2008

Stolle, C., Lühr, H., Rother, M., & Balasis, G. (2006). Magnetic signatures of equatorial spread F as observed by the CHAMP satellite. *Journal of Geophysical Research*, *111*, A02304. https://doi.org/10.1029/2005JA011184

Su, S. Y., Chao, C. K., & Liu, C. H. (2008). On monthly/seasonal/longitudinal variations of equatorial irregularity occurrences and their relationship with the postsunset vertical drift velocities. *Journal of Geophysical Research*, *113*, A05307. https://doi.org/10.1029/2007JA012809

Su, S. Y., Liu, C. H., Ho, H. H., & Chao, C. K. (2006). Distribution characteristics of topside ionospheric density irregularities: Equatorial versus midlatitude regions. *Journal of Geophysical Research*, *111*, A06305. https://doi.org/10.1029/2005ja011330

Tapping, K. F. (2013). The 10.7 cm solar radio flux (F10.7). *Space Weather-the International Journal of Research and Applications*, *11*(7), 394–406. https://doi.org/10.1002/swe.20064

Uma, G., Liu, J. Y., Chen, S. P., Sun, Y. Y., Brahmanandam, P. S., & Lin, C. H. (2012). A comparison of the equatorial spread F derived by the International Reference Ionosphere and the S4 index observed by FORMOSAT-3/COSMIC during the solar minimum period of 2007–2009. *Earth, Planets and Space*, *64*(6), 467–471. https://doi.org/10.5047/eps.2011.10.014

Wang, Z., Liu, H., Shi, J., Wang, G., & Wang, X. (2019). Plasma blobs concurrently observed with bubbles in the Asian-Oceanian sector during solar maximum. *Journal of Geophysical Research: Space Physics*, *124*, 7062–7071. https://doi.org/10.1029/2018JA026373

Woodman, R. F., & La Hoz, C. (1976). Radar observations of F region equatorial irregularities. *Journal of Geophysical Research*, *81*(31), 5447–5466. https://doi.org/10.1029/JA081i031p05447

Xiong, C., & Lühr, H. (2014). An empirical model of the auroral oval derived from CHAMP field-aligned current signatures—Part 2. *Annales Geophysicae*, *32*(6), 623–631. https://doi.org/10.5194/angeo-32-623-2014

Xiong, C., Park, J., Lühr, H., Stolle, C., & Ma, S. Y. (2010). Comparing plasma bubble occurrence rates at CHAMP and GRACE altitudes during high and low solar activity. *Annales Geophysicae*, *28*(9), 1647–1658. https://doi.org/10.5194/angeo-28-1647-2010

Xiong, C., Stolle, C., & Lühr, H. (2016). The Swarm satellite loss of GPS signal and its relation to ionospheric plasma irregularities. *Space Weather*, *14*, 563–577. https://doi.org/10.1002/2016SW001439

Xiong, C., Stolle, C., & Park, J. (2018). Climatology of GPS signal loss observed by Swarm satellites. *Annales Geophysicae*, *36*(2), 679–693. https://doi.org/10.5194/angeo-36-679-2018

Yeh, K. C., & Liu, C. H. (1982). Radiowave scintillations in the ionosphere. *Proceedings of the IEEE*, *70*(4), 324–360.